LAWRENCE
LIVERMORE
NATIONAL
LABORATORY

UCRL-JRNL-234373

The XRS microcalorimeter spectrometer at the Livermore Electron Beam Ion Trap

F. S. Porter, P. Beiersdorfer, K. Boyce, G. V. Brown, H. Chen, J. Gygax, S. M. Kahn, R. Kelley, C. A. Kilbourne, E. Magee, D. B. Thorn

September 7, 2007

Canadian Journal of Physics

The XRS microcalorimeter spectrometer at the Livermore Electron Beam Ion Trap

F. S. Porter[1], P. Beiersdorfer[2], K. R. Boyce[1], G. V. Brown[2], H. Chen[2], J. Gygax[1], S. M. Kahn[3], R. L. Kelley[1], C. A. Kilbourne[1], E. Magee[2], D. B. Thorn[2]

[1]NASA/GSFC, Greenbelt, MD 20771, USA
[2]Lawrence Livermore National Laboratory, Livermore, CA 94550, USA
[3]Department of Physics, Stanford University, Stanford, CA 94305, USA

Corresponding Author Address:

NASA/GSFC, Code 662
Building 2, Room S210
Greenbelt, MD 20771
Phone: 301-286-5016
FAX: 301-286-1684
Email: porter@milkyway.gsfc.nasa.gov

PACS: 52.25.Os, 52.70.La, 95.85.Nv, 32.30.Rj, 07.85.Fv, 78.70.En

Abstract:

NASA's X-ray Spectrometer (XRS) microcalorimeter instrument has been operating at the Electron Beam Ion Trap (EBIT) facility at Lawrence Livermore National Laboratory since July of 2000. The spectrometer is currently undergoing its third major upgrade to become an easy to use, extremely high performance instrument for a broad range of EBIT experiments. The spectrometer itself is broadband, capable of simultaneously operating from 0.1 to 12 keV and has been operated at up to 100 keV by manipulating its operating conditions. The spectral resolution closely follows the spaceflight version of the XRS, beginning at 10 eV FWHM at 6 keV in 2000, upgraded to 5.5 eV in 2003, and will hopefully be ~3.8 eV in the Fall of 2007. Here we review the operating principles of this unique instrument, the extraordinary science that has been performed at EBIT over the last 6 years, and prospects for future upgrades. Specifically we discuss upgrades to cover the high-energy band (to at least 100 keV) with a high quantum efficiency detector, and prospects for using a new superconducting detector to reach 0.8 eV resolution at 1 keV, and 2 eV at 6 keV with high counting rates.

Introduction to Microcalorimeters:

Non-dispersive x-ray spectrometers have distinct advantages for both spaceflight x-ray observatories and ground-based x-ray diagnostics. In general, they tend to be efficient, polarization insensitive, and broadband. However, most non-dispersive spectrometers based on gas proportional counters or solid state devices such as CCDs have severely limited spectral resolving power compared to crystal or grating dispersive systems.

In 1984 a new type of non-dispersive x-ray spectrometer was invented at NASA's Goddard Space Flight Center (GSFC) based on thermal x-ray detection at very low temperatures [1]. This conceptually simple detection scheme, shown in Fig. 1, uses a very low heat capacity x-ray absorber attached to a high sensitivity thermometer. When an x-ray is absorbed through photoabsorption or Compton scattering in the absorber, the primary photoelectron is quickly thermalized into the available excitation channels in the solid state system. For dielectric systems the photoelectron thermalizes into phonons, in a metallic system into a combination of phonons and electrons, and in a superconducting system it thermalizes into a combination of phonons and quasiparticles. The thermometer then measures the transient temperature increase of the device and the temperature is reset to the heat sink through a weak thermal link. The temperature excursion one expects from such a system is then simply:

$$\Delta T \approx \frac{E}{C(T)} \qquad (1)$$

where E is the energy deposited by the incident photon and C(T) is the heat capacity of the detector. The spectral resolving power of this type of detector is then only limited by the thermodynamic fluctuation noise due to phonon exchange across the weak thermal link. This is the fundamental limiting noise term for all thermal detectors and limits the energy resolution for an optimized detector as:

$$\Delta E \propto \sqrt{k_B T_0^2 C_0} \qquad (2)$$

where T_0 is the temperature of the heat bath and C_0 is the heat capacity at that temperature [1]. Theoretically, the resolving power of such a device has no upper limit, but is normally limited by practical considerations such as thermometer noise, amplifier noise, and materials properties. Early results with these detectors, termed an x-ray microcalorimeter, showed that a resolving power of 1000 at 6 keV was not impractical and recently resolving powers of 3000 at 6 keV [2] and 3000 at 60 keV (see Fig. 18) have been obtained. An introduction to x-ray microcalorimeters can be found in [3], a detailed description of the physics of microcalorimeter detectors can be found in [4] and [5], and their use in x-ray astrophysics in [6].

The x-ray microcalorimeter spectrometer has become an important tool for x-ray astrophysics. The fact that it is non-dispersive means that its energy resolution does not degrade with the spatial extent of the source. Most dispersive instruments are limited to nearly point-like objects since they are in-essence "slit-less" spectrometers. Thus an x-ray microcalorimeter instrument can be used to study spatially extended x-ray emitting objects such as supernova remnants, galaxies, galaxy clusters, and comets. In addition, the use of an imaging microcalorimeter detector array provides true spatial-spectral diagnostics unavailable using any other type of instrument. The large bandpass of the instrument, nominally 0.05 – 10 keV but extendable to more than 100 keV, allows simultaneous spectral coverage without difficult cross-instrument normalization. Finally, since the instrument is single photon counting, event timing and coordination with dynamics in the x-ray source is intrinsic to the instrument.

In the 23 years since we built the first x-ray microcalorimeter, we have constructed a number of spectrometers for both space flight and ground experiments. Our first flight instrument is the X-ray Quantum Calorimeter (XQC) rocket-borne suborbital spectrometer built in collaboration with the University of Wisconsin [7, 8]. The XQC is a 36 pixel microcalorimeter array with 1 mm^2 pixels operated at 60 mK using an adiabatic demagnetization refrigerator (ADR) and a 4 liter liquid helium bath. The spectrometer was built to measure the cosmic soft x-ray background from 0.02-1 keV and has a 1 steradian field of view and an energy resolution of ~9 eV at 1 keV. The XQC has flown three times in 1995, 1996 and 1999 and has shown that the soft x-ray background is dominated by K-shell transitions in highly ionized He-like and H-like oxygen that is almost certainly a superposition of local and non-local thermal plasmas and charge exchange between solar system neutrals and the solar wind [8]. We have recently developed and produced an improved detector system with 4 mm^2 pixels and an energy resolution of 5-6 eV FWHM at 1 keV for the next flight of the XQC. The new fully assembled flight detector is shown in Fig. 2.

The first orbital microcalorimeter instrument was the XRS (X-ray Spectrometer) system on the *Astro-E* and *Suzaku* (*Astro-E2*) observatories that were built as collaborations between Japan and the United States [9, 10]. The detector system for both of these instruments was a 32-pixel microcalorimeter array based on resistive implanted silicon thermistors and 8 μm thick HgTe x-ray absorbers. The *Astro-E*/XRS instrument had an energy resolution of 11 eV at 6 keV with a bandpass from below 0.1 to 10 keV. After the Astro-E satellite failed to achieve orbit, we re-designed the detector system to achieve higher performance [11] for the *Suzaku* observatory. The *Suzaku*/XRS detector system is shown in Fig. 3 and is comprised of a 6 x 6 detector array with 625x625x8 μm HgTe x-ray absorbers. The energy resolution of the flight detector system was 5-

6 eV FWHM at 6 keV with a bandpass of 0.1-10 keV during pre-flight testing. The XRS detector system was operated at 60 mK using a single stage ADR with precooler stages at 1.3 K using space-pumped liquid helium, 17K using solid Neon, and 60 K using a Stirling cycle cryo-cooler. The XRS achieved 7 eV FWHM at 6 keV on-orbit using an on-board calibration source. Unfortunately a design flaw in the accommodation of the instrument on the observatory caused an early termination of the 3 year experiment. The XRS instrument, however, performed flawlessly during its 6 weeks of on-orbit operation.

In our laboratory, we are currently developing detector systems targeted at the XMS (X-ray Microcalorimeter Spectrometer) for the *Constellation-X* observatory. This is planned to be a very large, 4096 pixel, microcalorimeter instrument with a 0.1-10 keV bandpass, an energy resolution of 2 eV at 6 keV, and the ability to handle up to 1 kcps/pixel. Our design for this system uses superconducting thermistors, termed Transition-Edge Sensors (TES), that are feedback biased in the middle of their superconducting transitions. The TES system results in a very high sensitivity thermometer over a narrow temperature range. The TES thermometers are coupled with in-situ deposited Bi/Au x-ray absorbers. We are currently producing 8x8 arrays of detectors using this system and have recently demonstrated 2.1 eV resolution at 6 keV [2].

The XRS/EBIT microcalorimeter instrument

In July, 2000, we delivered the first microcalorimeter array instrument to the Electron Beam Ion Trap (EBIT) facility at the Lawrence Livermore National Laboratory (LLNL). The EBIT is a plasma generator that uses an accelerated electron beam, an injected near-neutral target element(s), and a magnetic and electrostatic trap to produce a plasma with a well defined composition and ionization state. The EBIT system is described in detail elsewhere [12] including extensive description in this volume.

The microcalorimeter instrument, termed the XRS/EBIT, uses an engineering model detector system from the *Astro-E*/XRS program installed in a spare laboratory cryostat [13, 14]. The first generation XRS/EBIT instrument, shown in Fig. 4, had an energy resolution of 9-10 eV at 6 keV, a bandpass from 0.1-12 keV in its standard operating mode, and 10 μs event timing that is phase-synced to the EBIT timing pattern. We upgraded the system in October of 2003 to include the improved microcalorimeter detectors from the *Suzaku*/XRS program. The current XRS/EBIT instrument has an energy resolution of 5-6 eV at 6 keV using a 6 x 6 detector array fabricated on the same silicon wafer as the array in the *Suzaku*/XRS flight instrument. The XRS/EBIT microcalorimeter array is shown in Fig. 5. The array has 32 625x625x8 μm HgTe x-ray absorbers. The four corners of the array have 30 μm Bi absorbers that give an energy resolution of 70 eV FWHM at 60 keV on two of the channels and 150 eV on the other two. These early Bi high-energy absorbers yielded substantially lower performance than we expected. As we discuss later in this article, the 3rd generation microcalorimeter instrument at EBIT will use 100 μm HgTe absorbers that give 22 eV resolution at 100 keV with substantially increased quantum efficiency.

The XRS/EBIT cryostat uses a single stage ADR based on our XQC sounding rocket instrument to operate at 60 mK from a pumped liquid helium bath. The ADR runs for 12 hours at 60 mK between recharges and the liquid helium about 36 hours between fills. The cryostat runs either

vertically or horizontally using offset cryogen ports. Since the detector system looks out the bottom of the cryostat, the XRS/EBIT nominally operates horizontally when attached to the EBIT as shown in Figure 4. The XRS/EBIT aperture uses a series of three calibrated aluminum-on-polyimide infrared blocking filters to minimize heating of the detector system by environmental radiation, while maximizing the x-ray throughput at low energies [15]. The blocking filters, staged at 0.06, 1.5 and 77K, are composed of 500 Å of aluminum on 1000 Å of polyimide and are manufactured by Luxel [16].

The XRS/EBIT has operated nearly continuously at the EBIT facility at LLNL since the summer of 2000. Figures 6a-g demonstrate the performance of the instrument across its spectral band, showing the K-shell transitions from several He and H-like elements in the range from 0.4 to 12 keV. The XRS instrument on the Suzaku observatory was constructed principally to use the K-shell transitions of, for example, Fe as diagnostics of the plasma conditions in cosmic sources. Since, the XRS/EBIT is essentially identical to the XRS flight instrument, the results shown here represent the extraordinarily detailed spectral signatures that we would have seen from astrophysical sources had the XRS instrument continued to operate.

Laboratory Astrophysics with the XRS/EBIT:

The primary purpose of the XRS/EBIT spectrometer is in laboratory astrophysics. That is the production of astrophysical plasmas in the laboratory, a task for which the EBIT is uniquely suited, and the study of the subsequent x-ray emission. By varying the ionization state, equilibrium state, and elemental composition, we can relate the observed x-ray emission to the source conditions and translate this knowledge to observations of celestial sources. The phase space for the source parameters, however, is very large, particularly since cosmic sources are usually thermal plasmas with a wide distribution of electron energies. Thus spectral modeling of astrophysical plasmas requires spectral synthesis models based on detailed calculations of the atomic physics. It is impractical and unnecessary to provide a complete laboratory verification of the entire phase space of input parameters, but benchmarking the spectral synthesis models for carefully selected input conditions is key to enabling robust interpretation of the astrophysical spectra. This is the primary goal of our laboratory program.

Lawrence Livermore National Laboratory in collaboration with Columbia Univ., Stanford Univ., and NASA/GSFC has been using the EBIT for the production of laboratory astrophysical plasmas since the early 1990s. Extensive work has been done, for example, on wavelength determination, absolute electron impact excitation cross sections, and characterization of charge exchange recombination emission. The installation of the XRS/EBIT has added considerably to the laboratory astrophysics program by supplementing the existing solid state and dispersive spectrometers to give wide simultaneous bandpass coverage at relatively high spectral resolution. This is important for measuring absolute cross sections since the radiative recombination signature used to normalize the electron impact excitation cross sections occurs at a much higher energy and with 100x lower flux than the direct excitation emission as shown in Figure 7. It is important to note that most laboratory astrophysics experiments at the EBIT facility use a suite of simultaneous diagnostics. In particular, high-resolution crystal spectrometers are used to resolve line blends in the XRS/EBIT while the XRS/EBIT provides high efficiency and a broad bandpass. We have utilized this system to make extensive measurements of the emission cross

sections of L-shell transitions for Fe XVII-XXIV [17-21] and are preparing measurements for the other astrophysically important elements Ni, and C through Ca.

A unique and highly desirable feature of the XRS/EBIT is its ability to perform phase resolved spectroscopy with the EBIT. The EBIT is fundamentally a pulsed x-ray source. A typical EBIT cycle lasts from a few ms to a few 10s of seconds and consists of filling the trap, ionizing-up the trapped species to the target ionization state, and then a time period where the ionization state of the trapped ions is in equilibrium, but with a decaying flux as ions slowly escape the trap. The cycle is then repeated. An XRS/EBIT event stream is shown in Fig. 8 for a number of EBIT cycles. In a typical experiment many thousands of EBIT cycles are integrated to form an emission spectrum. However, it is important to synchronize the phase between the instrument and the EBIT and to perform phase resolved spectroscopy to isolate the equilibrium parts of the spectrum from the times when the ionization state is changing. Fig. 9 shows a phase resolved XRS/EBIT measurement of the entire EBIT timing cycle for 10,000 overlaid EBIT cycles. One can clearly see the plasma ionizing up from mostly Fe XVII through every intermediate charge state and finally settling into an equilibrium state dominated by Fe XXIII and XXIV. Fig. 10 shows the relative flux of dominant lines from several ionization species vs time, and Fig 11 shows the emission spectra at early and late ionization times. We note that precise phase-resolved spectroscopy is required to unambiguously interpret results from observations with the EBIT. Integrating spectrometers without event timing will lead to spurious results.

Interestingly, the ionization parameter for the EBIT is very similar to the ionization parameter characterizing the entire range of supernova remnants. The ionization parameter, measured in s-cm^{-3}, parameterizes the non-equilibrium state between the electron temperature and the degree of ionization of the ions [23]. Small ionization parameters indicate that the ions are still at a low ionization state compared to the equilibrium value based on the electron temperature. While the electron density in the EBIT is close to coronal densities near 10^{12} cm^{-3}, the time scale is fairly short. This produces an ionization parameter in the range from ~$5x10^{8}$ to ~$5x10^{12}$ s-cm^{-3}. We are thus able to study the non-equilibrium phase of material behind the shock-front in supernova remnants and to provide independent verification for the non-equilibrium spectral synthesis models currently used to interpret these observations.

Charge exchange recombination, where a highly charged ion passing through near neutral material captures an electron, is becoming increasingly important in interpreting astrophysical spectra [23]. X-ray emission due to charge exchange is believed to exist in comets, short and long-term enhancements to the soft cosmic x-ray background, interactions between shock-heated plasmas and molecular clouds in supernova remnants, and perhaps x-ray emission from the galactic center. The XRS/EBIT has played a substantial role in understanding the spectral signature of charge exchange emission under a variety of plasma conditions. The EBIT produces charge exchange recombination by first trapping and ionizing a plasma of the receptor species and then turning off the electron beam. Without the electron beam, the plasma is no longer radially confined and fills the trap volume. The plasma then recombines with neutrals that are separately injected into the trap. The 1000x lower x-ray flux compared to collisionally excited emission and the lack of radial confinement and thus an effective “slit” makes dispersive spectrometers impractical for charge exchange measurements. The XRS/EBIT, however, is nearly the ideal choice. Since it is a non-dispersive spectrometer its spectral resolution does not

depend on the source extent, and the high-efficiency of the detector makes the low-flux observations practical in a finite observation. Fig. 12 shows a phase resolved observation of charge exchange with highly ionized oxygen showing the high contrast measurement, and Figure 13 the resultant spectrum for a 48 ks observation. The spectrum in Fig. 13 shows the telltale signature of charge exchange emission in the distinctly non-thermal enhancement of the high Rydberg transitions.

We have successfully used the XRS/EBIT to make a number of important measurements of charge exchange including a full laboratory simulation of the emission from comet C/1999 S4 as observed with the *Chandra* X-ray observatory [24]. This measurement is one of the key demonstrations that cometary x-ray emission is produced by charge exchange. Another key result from the XRS/EBIT is that charge exchange spectra are dependent not just on the species of the ions and the relative velocity of the interaction but is also dependent on the donor species [24]. This result demonstrates that observations of astrophysical charge exchange are highly diagnostic. Using a high resolution, non-dispersive spectrometer like the XRS/EBIT one can determine the ion species, ionization state, donor species and ionization state, and the relative velocity of the interaction. Thus, for example, we can use the solar wind as the ion source to, in principle, remotely probe the distribution and state of neutral material throughout the solar system including comets, planetary atmospheres, heliospheric gas, and the geotail. The lack of continuum emission in charge-exchange dominated spectra makes these measurements relatively simple to interpret. Fig. 14 shows a simulation, based on cross sections [25], of only a 500 s observation using the proposed *Constellation-X* observatory. The XRS/EBIT and the EBIT facility will continue to play a key role in interpreting these measurements and will be critically important in interpreting the data from the next generation of x-ray observatories.

Finally, the XRS/EBIT has been used extensively to study hard x-ray and gamma ray emission at energies up to 60 keV. A recent example is the observation of a low-lying nuclear state in ^{229}Th using the XRS/EBIT [26]. This measurement was made using the cascade shown in Fig. 15 and a differencing scheme, measuring gamma ray emission at 29 and 42 keV from the decay of ^{233}U to ^{229}Th. To extend the bandpass of the XRS/EBIT to higher energies without modifying the detector electronics, we operated the detector array at 90 mK, reducing the sensitivity of the thermometers and increasing the heat capacity of the detectors. In this mode, we achieved an energy resolution of 26 eV at 60 keV, although with a fairly low quantum efficiency due to the low stopping power of the 8 μm thick x-ray absorbers. To compensate for the low quantum efficiency, the ^{233}U source was placed inside the cryostat, about 1 cm in front of the detector. The result of these measurements was a precise determination of the lowest lying observed nuclear state of 7.6 +/- 0.5 eV above the ground state in ^{229}Th with important implications to such diverse fields as general relativity, quantum computing, and the variability of physical constants [27].

The EBIT Calorimeter Spectrometer (ECS): The 3rd generation microcalorimeter spectrometer at EBIT

The XRS/EBIT was built quickly, over a four month period in early 2000 from available resources in our laboratory. It is a difficult system to operate, requiring relatively frequent ADR cycles and cryogen fills, and the added complexity of a pumped liquid helium bath. We are

currently completing a facility class instrument, the EBIT Calorimeter Spectrometer (ECS), to replace the XRS/EBIT at the EBIT facility at LLNL. The ECS spectrometer is a low maintenance, high performance microcalorimeter spectrometer that incorporates a new type of refrigeration system developed at NASA/GSFC and an improved detector system that allows the same Suzaku/XRS detector array to operate with higher spectral resolution and much larger band pass with significantly higher quantum efficiency. The ECS spectrometer is in its final phase of construction and will be delivered to the EBIT facility in the fall of 2007.

The ECS spectrometer uses a single stage adiabatic demagnetization refrigerator with a 100g ferric ammonium alum refrigerant and a 40 kG superconducting magnet. The ADR is precooled using a completely self-contained ^{3}He/^{4}He sorption pumped refrigerator constructed by Chase Cryogenics [28]. This was chosen over a more traditional two stage ADR due to the ~100 μW of heat generated at the detector housing from the 130K jFET preamplifiers in the XRS design [29]. The ^{3}He/^{4}He sorption cooler provides substantial cooling power at 340 mK which is used to cool the outer detector housing and to precool the ADR during the heat rejection part of the cooling cycle. The heat of magnetization in the salt pill is rejected to the sorption cooler using a passive gas-gap heat switch. The end result is a compact, high performance, high duty cycle refrigeration and detector system package as shown in Fig. 16.

The ECS cryogenics package is completely self-contained, requiring no external plumbing and simply a thermal interface below 5K to operate. In the ECS cryostat the thermal interface is provided by an atmospheric liquid helium bath at 4.2 K but we are currently constructing a cryogen-free system in our laboratory that will use an identical refrigeration package. The ECS detector system in its first test run operated at 50 mK for 54 hours before the sorption cooler needed to be recharged. Minor modifications to the detector system support structure will allow the system to operate for over 70 hours with a two hour recycle time giving a duty cycle of 97%. The ADR itself has very low parasitic power due to the 340 mK interface temperature. Even with the relatively high off-conductance of the gas-gap heat switch, we measure the parasitic load on the ADR at only 54 nW. The duty cycle of the refrigerator is entirely limited by the 15 J cooling capacity of the He-3 stage. The ECS uses a 32-liter unpumped liquid helium bath with a hold time in excess of 14 days, and a 25 liter liquid nitrogen bath with a hold time in excess of 7 days. The ECS refrigeration package automatically recycles under software control every three days in the middle of the night. The end result is a low maintenance instrument for long-term use at the EBIT facility at LLNL.

The detector system in the ECS has also undergone substantial improvements. We have recently demonstrated [30] that reducing the operating temperature and optimizing the bias point of a standard XRS detector array can improve the energy resolution to 3.7 eV as shown in Fig 17. Further we have shown that using thinly diced, commercially produced 0.5 mm thick HgTe wafers, we can fabricate 100 μm thick x-ray absorbers that give 22 eV resolution at 60 keV with almost 30% quantum efficiency at 60 keV as shown in Fig. 18. We are currently producing the final detector array for the ECS instrument that will be based on another detector array from the Suzaku/XRS flight wafer. We will use a hybrid checkerboard absorber scheme where every other pixel is a mid-energy 625x625x8 μm HgTe absorber interspersed with high-energy 625x500x100 μm HgTe absorbers. This is predicted to give a simultaneous high resolution band pass of <0.1-

12 keV with a resolution of below 4 eV at 6 keV and 0.5-100 keV with a resolution of below 25 eV at 60 keV.

The future 4th generation microcalorimeter instrument at EBIT

The next generation of x-ray observatories including *Constellation-X*, *NeXT*, and *XEUS* will include very high-resolution x-ray spectrometers with resolving powers of up to 3000 across a bandpass from 0.1-10 keV. This will produce extraordinary demands on our knowledge of the atomic physics that is used to model the complex astrophysical observations. In the past, our measurements of simulated astrophysical plasmas in the laboratory have been key to refining our understanding of the limits of the current spectral synthesis models and for guiding the atomic physics calculations used to improve these models. The ECS spectrometer we are about to install at the EBIT facility at LLNL will continue this process for the next several years. However the performance of the next generation of observatories will drive us to make measurements on the ground with, minimally, the same precision as the orbital observatories. We have thus recently proposed a 4th generation microcalorimeter system for the EBIT facility based on the same technology we are developing for the *Constellation-X* observatory.

We have recently demonstrated a Transition Edge Sensor (TES) microcalorimeter array with 2.1 eV resolution at 6 keV [Ref Naoko], and have produced a hybrid low/mid detector array that is predicted to have 0.8 eV resolution at 1 keV on absorber-less detectors. In addition, NIST/Boulder has produced a high-energy TES detector array with 25 eV resolution at 100 keV and 70% quantum efficiency (QE) at 60 keV [31]. The 4th generation EBIT microcalorimeter instrument, termed the Transition Edge Microcalorimeter Spectrometer (TEMS) will be based on these developments. We have proposed to build a cryogen-free spectrometer using the refrigeration package developed for the ECS spectrometer and a hybrid focal plane consisting of a 16x16 low/mid energy checkerboard hybrid array and an 8x8 high energy array. The readout will use advanced superconducting multiplexer electronics developed at NIST [32]. The predicted performance of the spectrometer is 0.8 eV FWHM with a bandpass from 0.02-1 keV, 2.0 eV FWHM from 0.05-10 keV with 95% QE at 6 keV, and ~25 eV FWHM from 0.5-100 keV with 70% QE at 60 keV.

Summary

Over the last 6 years, microcalorimeter spectrometers have made important scientific contributions to our understanding of astrophysical observations, through our laboratory astrophysics program at the EBIT facility at LLNL. The original XRS/EBIT instrument, based on a spare detector system from the *Astro-E*/XRS flight system, has been in nearly continuous operation since the summer of 2000. In 2003 the XRS/EBIT was significantly upgraded to use the improved detector system from the *Suzaku*/XRS flight instrument. We are currently performing the final assembly of the ECS spectrometer that will be the 3rd generation microcalorimeter spectrometer at the EBIT facility. The ECS spectrometer will be an easy to use facility-class instrument that will be a primary contributor to future laboratory astrophysics measurements. Finally, we have recently proposed to bring the most advanced x-ray detector technology to our laboratory astrophysics program, utilizing the substantial investment of the *Constellation-X* observatory program in microcalorimeters with superconducting thermistors.

The resulting TEMS spectrometer will bring the same high resolution, broadband capability to our laboratory program as will be achieved in the next generation of orbiting x-ray observatories.

Work by the University of California, LLNL was performed under the auspices of the Department of Energy under contract W-7405-Eng-48.

References:

1. S. H. Moseley, J. C. Mather, D. McCammon. J. Appl. Phys. 56, 1257 (1984).

2. N. Iyomoto et al., in preperation.

3. C. K. Stahle, D. McCammon, K. D. Irwin. Phys. Today. 52, 32 (1999).

4. J. C. Mather. Appl. Opt. 21, 1125 (1982).

5. D. McCammon. *In* Cryogenic Particle Detection. *Edited by* C. Enss. Springer, Heidelberg. 2005. p. 1.

6. F. S. Porter, G. V. Brown, J. Cottam. *In* Cryogenic Particle Detection. *Edited by* C. Enss. Springer, Heidelberg. 2005. p. 359.

7. F. S. Porter, R. Almy, E. Apodaca, E. Figueroa-Feliciano, M. Galeazzi, R. Kelley, D. McCammon, C. K. Stahle, A. E. Szymkowiak, W. T. Sanders. Nucl. Inst. And Meth. A. 444, 175 (2000).

8. D. McCammon, R. Almy, E. Apodaca, W. Bergmann Tiest, W. Cui, S. Deiker, M. Galeazzi, M. Juda, A. Lesser, T. Mihara, J. P. Morgethaler, W. T. Sanders, J. Zang, E. Figueroa-Feliciano, R. L. Kelley, S. H. Moseley, R. F. Mushotzky, F. S. Porter, C. K. Stahle, A. E. Szymkowiak. ApJ. 576, 188 (2002).

9. R. L. Kelley, K. Mitsuda, C. A. Allen, P. Arsenovic, M. D. Audley, T. G. Bialas, K. R. Boyce, R. F. Boyle, S. R. Breon, G. V. Brown, J. Cottam, M. J. Dipirro, R. Fujimoto, T. Furusho, K. C. Gendreau, G. G. Gochar, O. Gonzalez, M. Hirabayashi, S. S. Holt, H. Inoue, M. Ishida, Y. Ishisaki, C. S. Jones, R. Keski-Kuha, C. A. Kilbourne, D. McCammon, U. Morita, S. H. Moseley, B. Mott, K. Narasaki, Y. Ogawara, T. Ohashi, N. Ota, J. S. Panek, F. S. Porter, A. Serlemitsos, P. J. Shirron, G. A. Sneiderman, A. E. Szymkowiak, Y. Takei, J. L. Tveekrem, S. M. Volz, M. Yamamoto, N. Y. Yamasaki. PASJ. 59, 77 (2007).

10. K. Mitsuda et al., PASJ. 59, 1 (2007).

11. C. K. Stahle, C. A. Allen, K. R. Boyce, R. P. Brekosky, G. V. Brown, J. Cottam, E. Figueroa-Feliciano, M. Galeazzi, J. D. Gygax, M. B. Jacobson, R. L. Kelley, D. Liu, D. McCammon, R. A. McClanahan, S. H. Moseley, F. S. Porter, L. E. Rocks, A. E. Szymkowiak, J. E. Vaillancourt. Nucl. Inst. and Meth. A. 520, 466 (2004).

12. M. A. Levine, R. E. Marrs, J. R. Henderson, D. A. Knapp, M. B. Schneider. Phys. Scr. T22, 157 (1988).

13. F. S. Porter, M. D. Audley, P. Beiersdorfer, K. R. Boyce, R. P. Brekosky, G. V. Brown, K. C. Gendreau, J. D. Gygax, S. M. Kahn, R. L. Kelley, C. K. Stahle, A. E. Szymkowiak. Proc. SPIE. 4140, 407 (2000).

14. F. S. Porter, G. V. Brown, K. R. Boyce, R. L. Kelley, C. A. Kilbourne, P. Beidersdorfer, H. Chen, S. Terracol, S. M. Kahn, A. E. Szymkowiak. Rev. Sci. Inst. 75, 3772 (2004).

15. M. D. Audley, K. A. Arnaud, K. C. Gendreau. K. R. Boyce, C. M. Fleetwood, R. L. Kelley, R. A. Keski-Kuha, F. S. Porter, C. K. Stahle, A. E. Szymkowiak, J. L. Tveekrem, R. Fuhimoto, K. Mitsuda, Y. Ishisaki, T. Mihara. Proc. SPIE 3765, 751 (1999).

16. Luxel Corporation, P. O. Box 1879, Friday Harbor, WA 98250.

17. H. Chen, P. Beiersdorfer, G. V. Brown, K. C. Gendreau, K. R. Boyce, R. L. Kelley, F. S. Porter, C. K. Stahle, A. E. Szymkowiak, S. M. Kahn, J.~Scofield. Astrophys. J. Lett. 567, L169 (2002).

18. H. Chen, P. Beiersdorfer, J. H. Scofield, G. V. Brown, K. R. Boyce, R. L. Kelley, C. A. Kilbourne, F. S. Porter, M. F. Gu, S. M. Kahn. ApJ. 618, 1086 (2005).

19. H. Chen, M. F. Gu, P. Beiersdorfer, K. R. Boyce, G. V. Brown, S. M. Kahn, R. L. Kelley, C. A. Kilbourne, F. S. Porter, J. H. Scofield. ApJ. 646, 653 (2006).

20. M. J. May, P. Beiersdorfer, N. Jordan, J. H. Scofield, K. J. Reed, S. B. Hansen, K. B. Fournier, M. F. Gu, G. V. Brown, F. S. Porter, R. Kelley, C. A. Kilbourne, K. R. Boyce. Nuclear Instruments and Methods in Physics Research B. 235, 231 (2005).

21. G. V. Brown, P. Beiersdorfer, K. R. Boyce, H. Chen, R. L. Kelley, C. A. Kilbourne, F. S. Porter, A. E. Szymkowiak, M. F. Gu, and S. M. Kahn. Phys. Rev. Lett., 96, 253201 (2006).

22. K. J. Borkowski, W. J. Lyerly, S. P. Reynolds. ApJ. 548, 820 (2001).

23. T. E. Cravens. Science. 296, 1042 (2002).

24. P. Beiersdorfer, K. R. Boyce, G. V. Brown, H. Chen, S. M. Kahn, R. L. Kelley, M. May, R. E. Olson, F. S. Porter, C. K. Stahle, W. A. Tillotson. Science. 300, 1558 (2003).

25. D. Bodewits, D. J. Christian, M. Torney, M. Dryer, C. M. Lisse, K. Dennerl, T. H. Zurbuchen, S. J. Wolk, A. G. G. M. Tielens, R. Hoekstra. Astronomy and Astrophysics. Submitted

26. B. R. Beck, J. A. Becker, P. Beiersdorfer, G. V. Brown, K. J. Moody, J. B. Wilhelmy, F. S. Porter, C. A. Kilbourne, R. L. Kelley. Phys. Rev. Lett. 98, 142501 (2007).

27. E. Peik and C. Tamm, Europhys. Lett. **61**, 181 (2003).

28. Chase Research Cryogenics Ltd., Uplands, 140 Manchester Road, Sheffield S10 5DL, UK.

29. F. S. Porter, M. D. Audley, R. P. Brekosky, R. J. Derro, M. J. Dipirro, K. C. Gendreau, J. D. Gygax, R. L. Kelley, D. McCammon, A. Morrel, S. D. Murphy, R. J. Paulos, T. Pham, C. K. Stahle, A. E. Szymkowiak, J. G. Tuttle. Proc. SPIE. 3765, 729 (1999).

30. F. S. Porter, R. L. Kelley, C. A. Kilbourne. Nucl. Inst. and Meth. A. 559, 436 (2006).

31. B. L. Zink, J. N. Ullom, J. A. Beall, K. D. Irwin, W. B. Dorese, W. D. Duncan, L. Ferreira, G. C. Hilton, R. D. Horansky, C. D. Reintsema, L. R. Vale. Appl. Phys. Lett. 89, 124101 (2006).

32. W. B. Dorese, J. A. Beall, S. Deiker, W. D. Duncan, L. Ferreira, G. C. Hilton, K. D. Irwin, C. D. Reintsema, J. N. Ullom, L. R. Vale, Y. Xu. Appl. Phys. Lett. 85, 4762 (2004).

Figure captions:

1. Functional diagram of a thermal x-ray detector. The x-ray is absorbed into a high opacity, low heat capacity x-ray absorber, the transient thermal signature is characterized with a high sensitivity thermometer, and then the temperature is reset to a thermal bath through a weak thermal link.

2. A photograph of the new XQC flight microcalorimeter detector array mounted in its detector housing. The XQC detector is a 6x6 array of microcalorimeter detectors with 2000 x 2000 x 0.8 μm HgTe absorbers.

3. An optical micrograph of the partially assembled XRS flight microcalorimeter array. The detectors on the lower left show bare pixels with their circular absorber mounting tabs and the curved mechanical supports which serve as the weak thermal link to the heat sink. The detectors in the center and upper right have their 625x625x8 μm HgTe absorbers attached.

4. A photograph of the XRS/EBIT instrument, oriented horizontally in the bottom center, attached to the EBIT instrument (back, left) at the EBIT facility at LLNL.

5. The XRS/EBIT detector array installed in its detector assembly. The array is composed of 32 625x625x8 μm HgTe absorbers and four 30 μm Bi high-energy absorbers at the four corners of the array. The Bi absorbers are the gray squares towards the middle of the detector dice.

6. XRS/EBIT spectra of K-shell emission of highly ionized elements injected into the EBIT: (a) O XVII/OVIII, (b) Ne IX/X, (c) S XV, (d) Ar XVII/XVIII, (e) Fe XXV/XXVI, (f) Ni XXVII/XXVIII, and (g) Kr XXXV.

7. XRS/EBIT spectrum of Fe XVII showing the electron impact excitation and (inset) the 200 times weaker radiative recombination (RR) emission.

8. XRS/EBIT measurement of photon energy vs time for 10 EBIT Fe injection cycles. Each cross in the figure is an individual photon measured with the XRS/EBIT. Each EBIT cycle typically consists of filling the trap, ionizing-up the trapped species to the target ionization state, and then a time period where the ionization state of the trapped ions is in equilibrium.

9. (a) XRS/EBIT phase resolved energy vs. EBIT injection time for 10,000 EBIT cycles and (b) a zoomed in portion of the first 200 ms of the 5 second EBIT cycle. One can clearly see the non-equilibrium part of the EBIT cycle where the charge state of the Fe ions is increasing before reaching a steady state value around 200 ms after injection.

10. Intensity vs. time plot from figure 9 of diagnostic lines from several Fe ionization states showing that the plasma consists of mostly Fe XVII at very early phase times and comes into equilibrium consisting mostly of Fe XXIII and XXIV for this particular electron beam energy (4.5 keV).

11. Spectra for two different EBIT phase times of the data from figure 9. (a) 10ms after Fe injection with an ionization parameter of $5x10^{9}$ s-cm^{-3} and (b) in equilibrium with an ionization time > $1x10^{11}$ s-cm^{-3}. Data taken with the first generation XRS/EBIT with 10 eV resolution at 6 keV.

12. Phase resolved photon energy vs. EBIT cycle time for a charge exchange experiment measured with the XRS/EBIT. In this experiment the electron beam is turned off at 0.2 seconds and the plasma is allowed to recombine through charge exchange for the remainder of the cycle. One can clearly see the 1000x weaker intensity of the charge exchange emission compared to the direct excitation.

13. Charge exchange spectrum of O VIII measured with the first generation XRS/EBIT. The spectrum shows the distinctly non-thermal line ratios in the high-Rydberg characteristic of charge exchange emission.

14. A simulated 500 s observation of charge exchange emission from a comet using the proposed *Constellation-X*/XMS instrument. The spectrum shows the extraordinary signal to noise achievable with a high resolution instrument in the absence of broad-band continuum. The simulation uses the observed fluxes from a Suzaku observation of comet 73P/SW3-C at 0.2 AU and charge exchange cross sections from [25].

15. Nuclear cascade for the decay of ^{233}U to ^{229Th} showing the gamma ray energies, in keV, of the emission. The energy of the ~0.008 keV state is derived by measuring the differences between the two decay paths from the 71.82 keV J=7/2 state using the XRS/EBIT.

16. The modular refrigeration and microcalorimeter detector system package in the new ECS spectrometer. The ^{3}He/^{4}He sorption pre-cooler is in the left foreground, the ADR is in the background behind the sorption cooler and the detector module is in the upper right with the aperture to the right in the photograph. The length scale of the photograph is about 35 cm horizontally.

17. The emission spectrum for a ^{55}Fe radioactive source measured with a standard XRS microcalorimeter detector cooled to 50 mK and using 180 MΩ load resistors. The instrumental broadening of the natural line shape is fit to be 3.76 eV FWHM. We expect similar performance for the final detector array to be installed in the ECS spectrometer.

18. The emission spectrum for an ^{241}Am source measured with a 500x500x100 μm high-energy HgTe absorber on a standard XRS microcalorimeter detector. The instrumental response is measured at 22 eV FWHM with 30% quantum efficiency at 60 keV. We expect similar performance for the high-energy pixels in the final ECS detector array.

Figure 1:

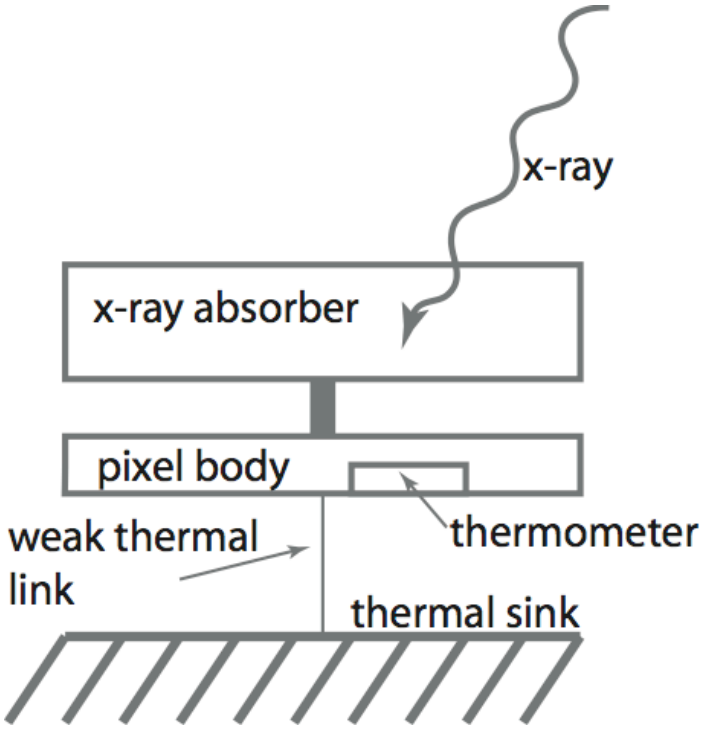
x-ray
x-ray absorber
pixel body
thermometer
weak thermal
link
thermal sink

Figure 2:

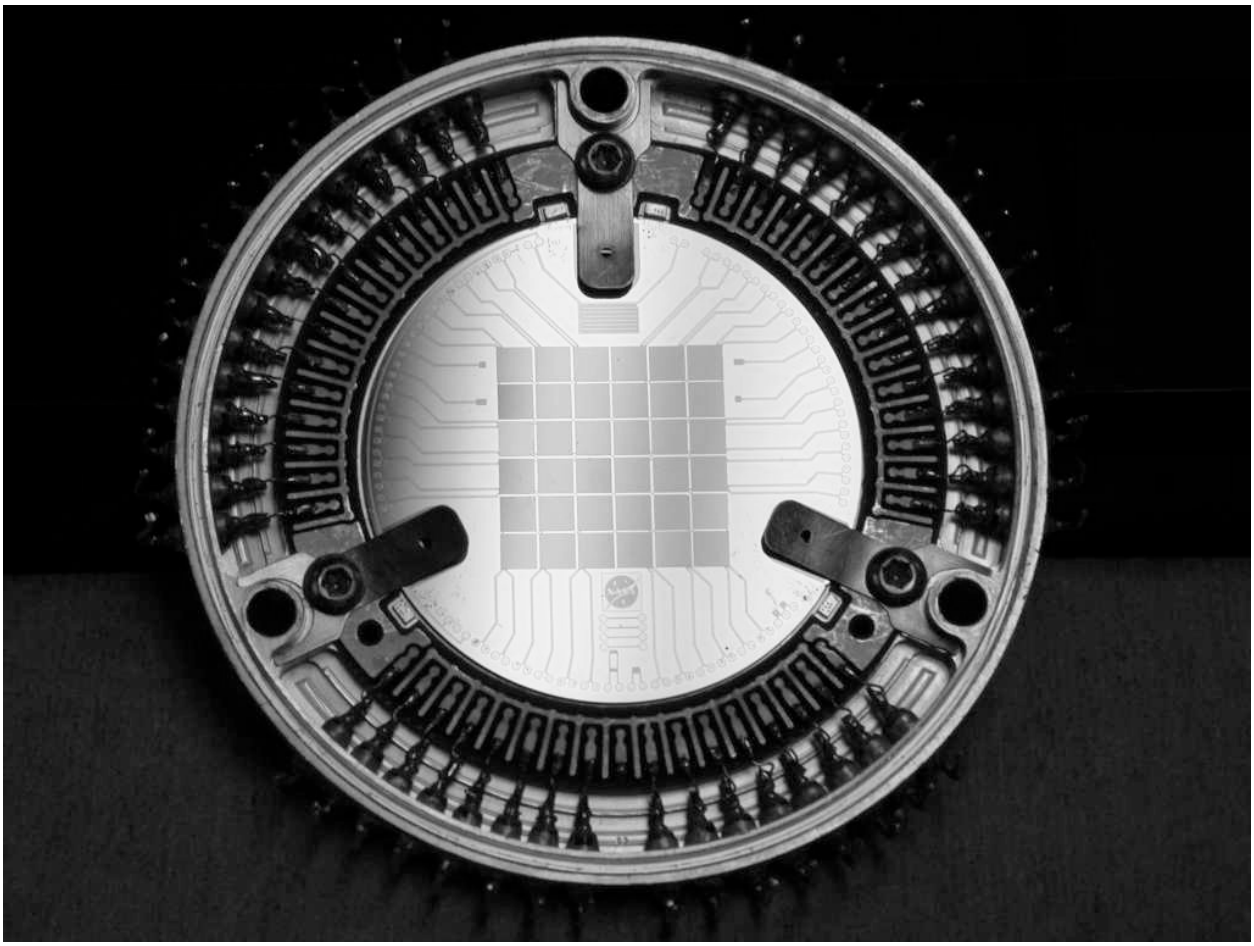

Figure 3:

Figure 4:

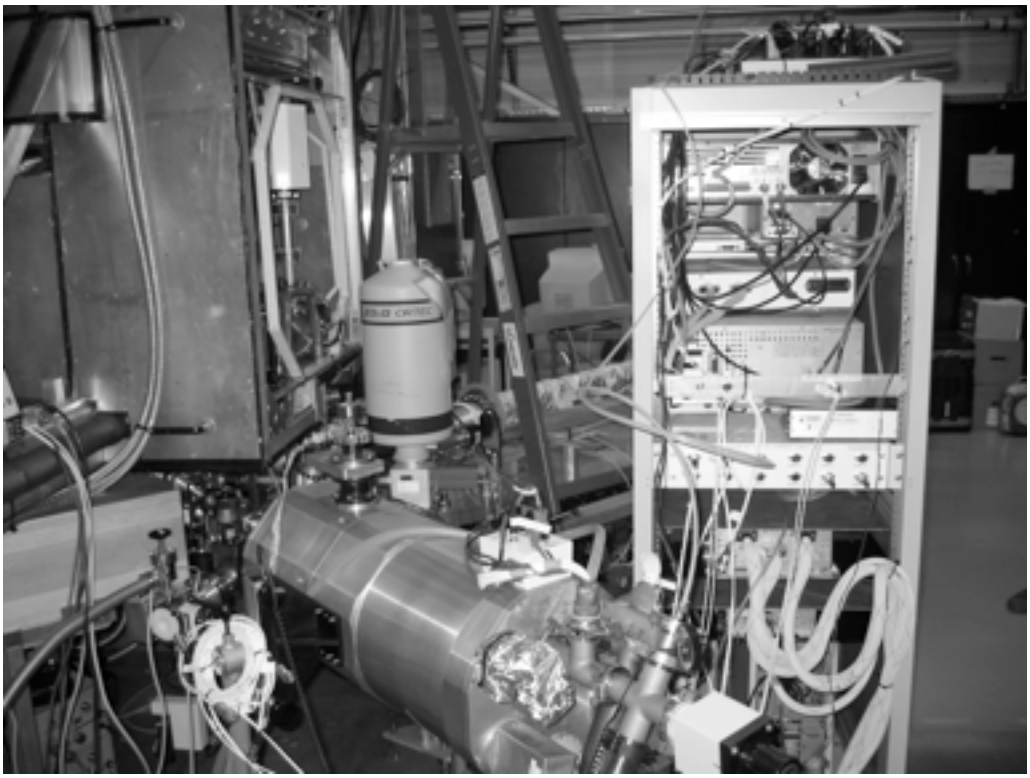

Figure 5:

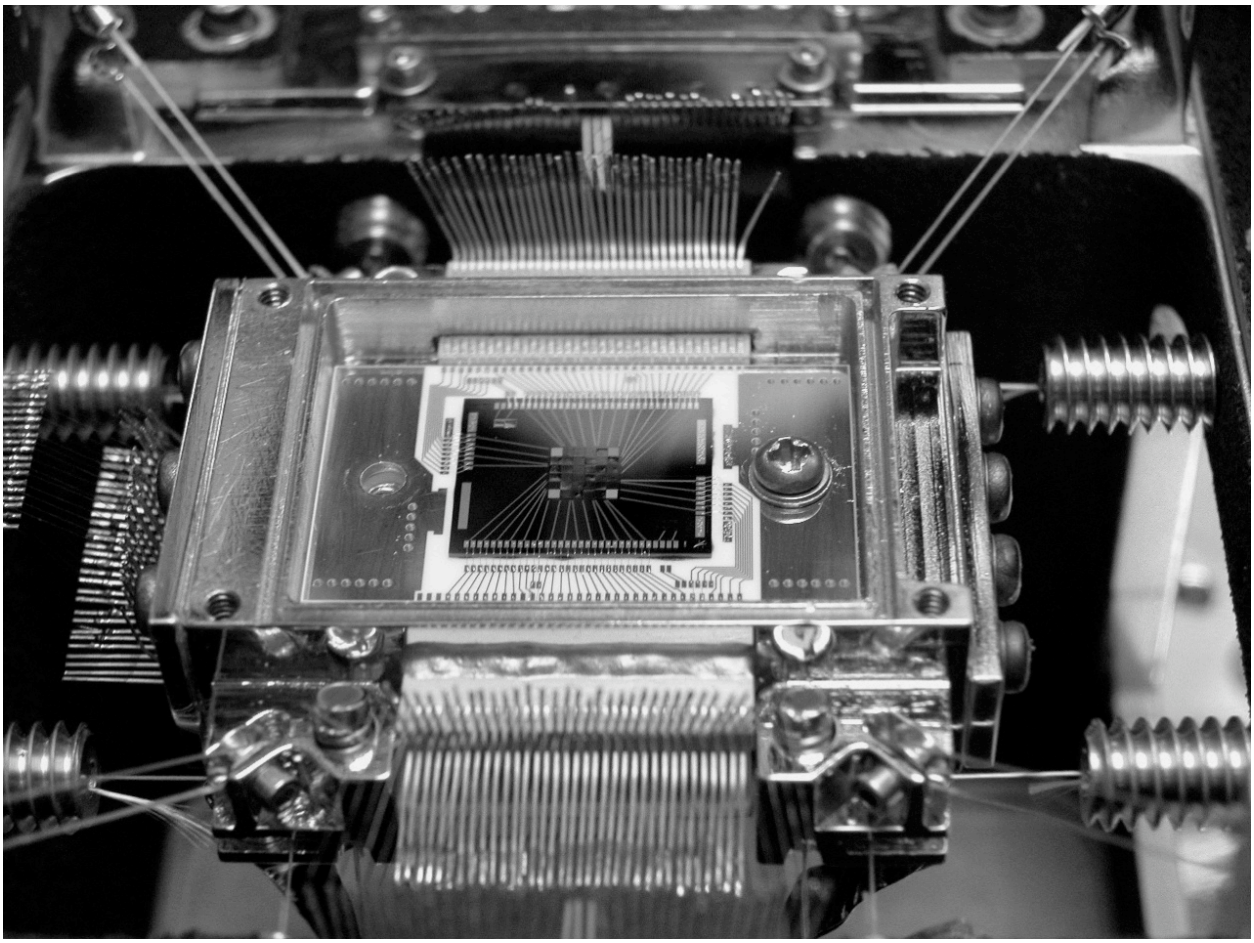

Figure 6 a-d:

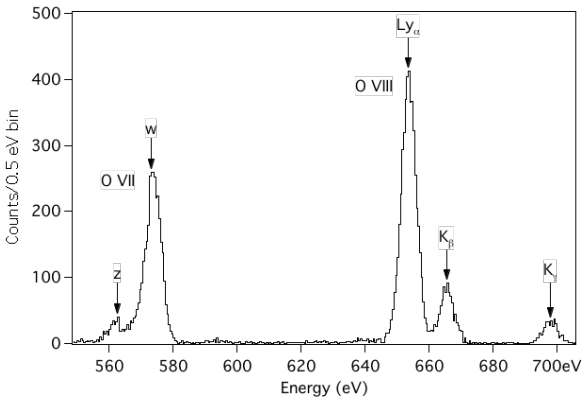
Counts/0.5 eV bin
Energy (eV)
O VII
O VIII
Ly$_\alpha$
K$_\beta$
K$_\gamma$
w
z

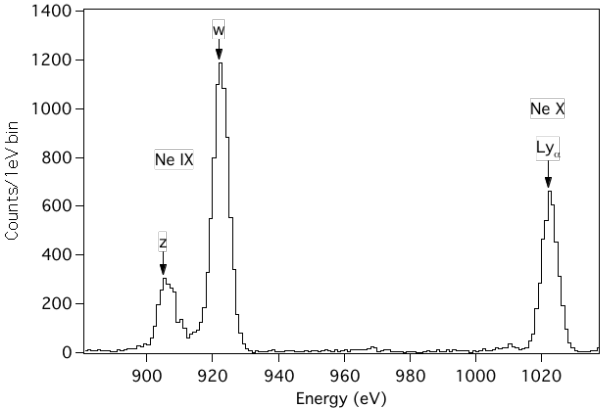
Counts/1eV bin
Energy (eV)
Ne IX
Ne X
Ly$_\alpha$
w
z

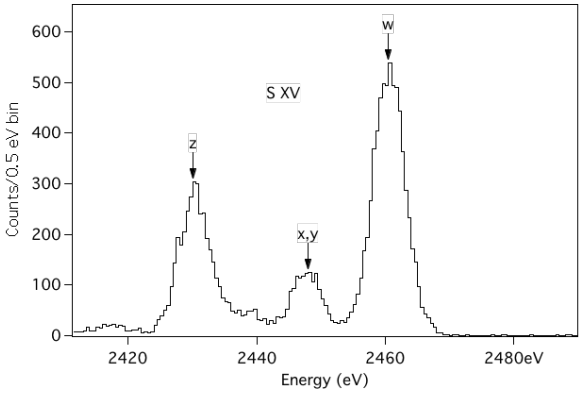
Counts/0.5 eV bin
Energy (eV)
S XV
w
z
x,y

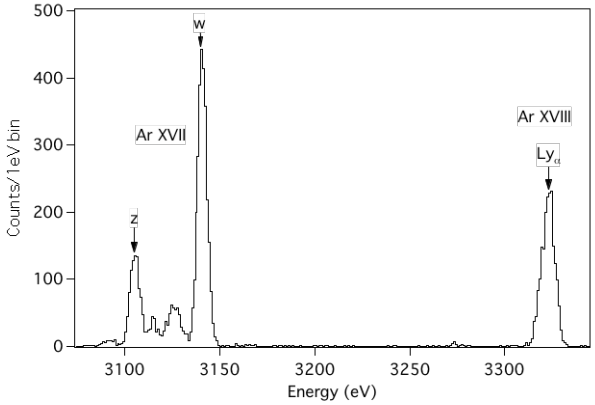
Counts/1eV bin
Energy (eV)
Ar XVII
Ar XVIII
Ly$_\alpha$
w
z

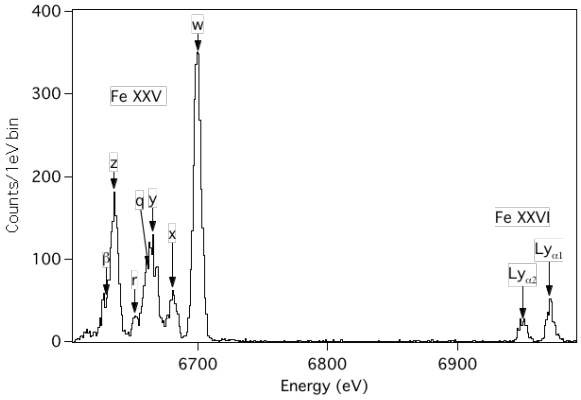
Counts/1eV bin
Energy (eV)
Fe XXV
Fe XXVI
Ly$_{\alpha1}$
Ly$_{\alpha2}$
w
z
q
y
x
r

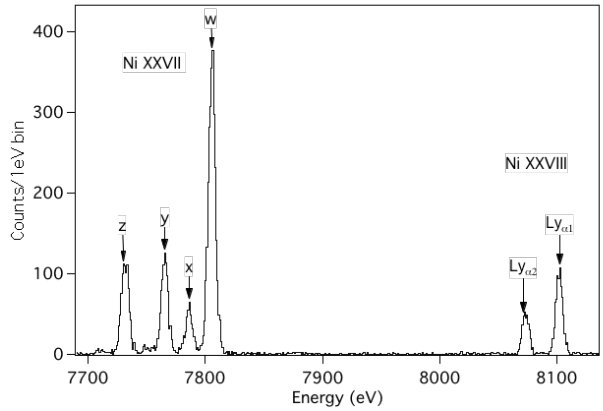
Counts/1eV bin
Energy (eV)
Ni XXVII
Ni XXVIII
Ly$_{\alpha1}$
Ly$_{\alpha2}$
w
z
y
x

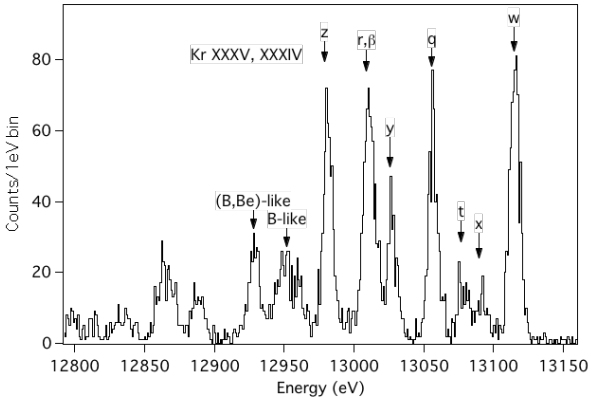
Counts/1eV bin
Energy (eV)
Kr XXXV, XXXIV
(B,Be)-like
B-like
z
r,β
q
w
y
t
x

Figure 7:

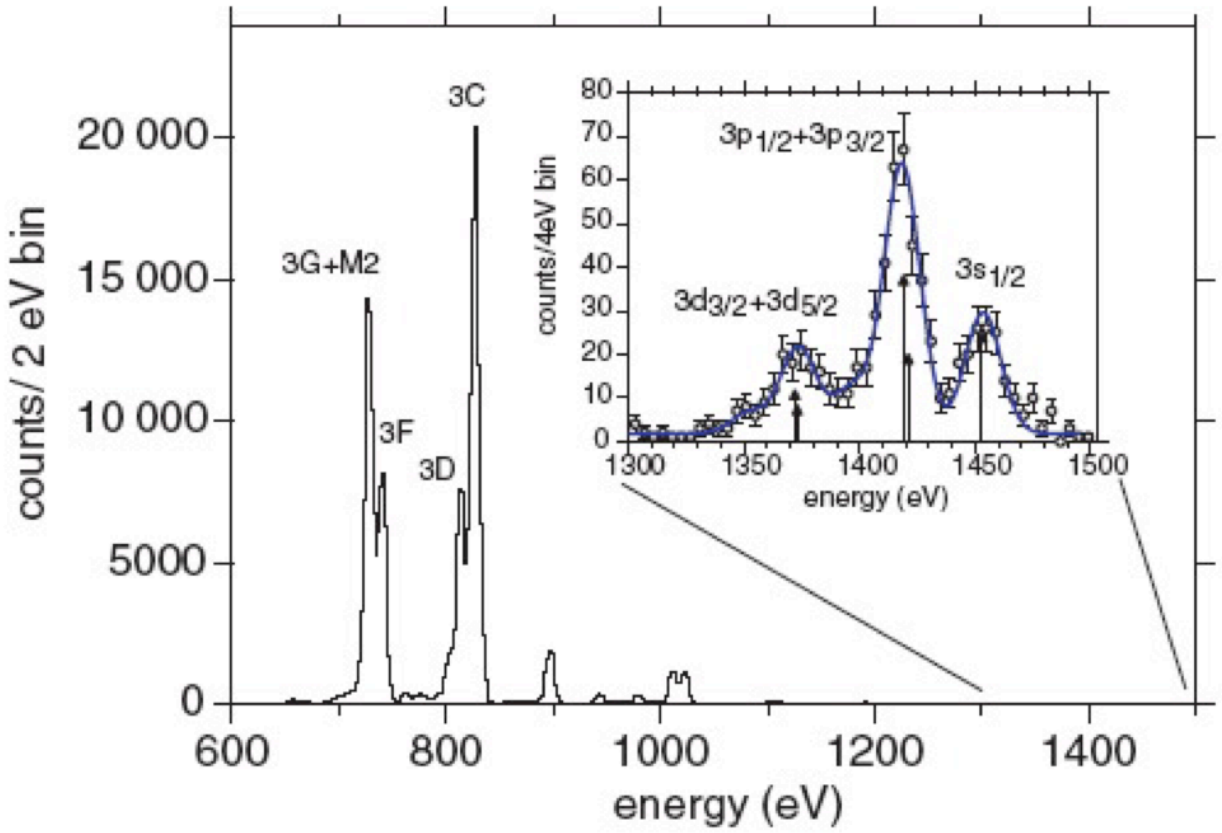
counts/ 2 eV bin
20 000
15 000
10 000
5000
0
600
800
1000
1200
1400
energy (eV)
3G+M2
3F
3D
3C
counts/4eV bin
80
70
60
50
40
30
20
10
0
1300
1350
1400
1450
1500
energy (eV)
3p1/2+3p3/2
3s1/2
3d3/2+3d5/2

Figure 8:

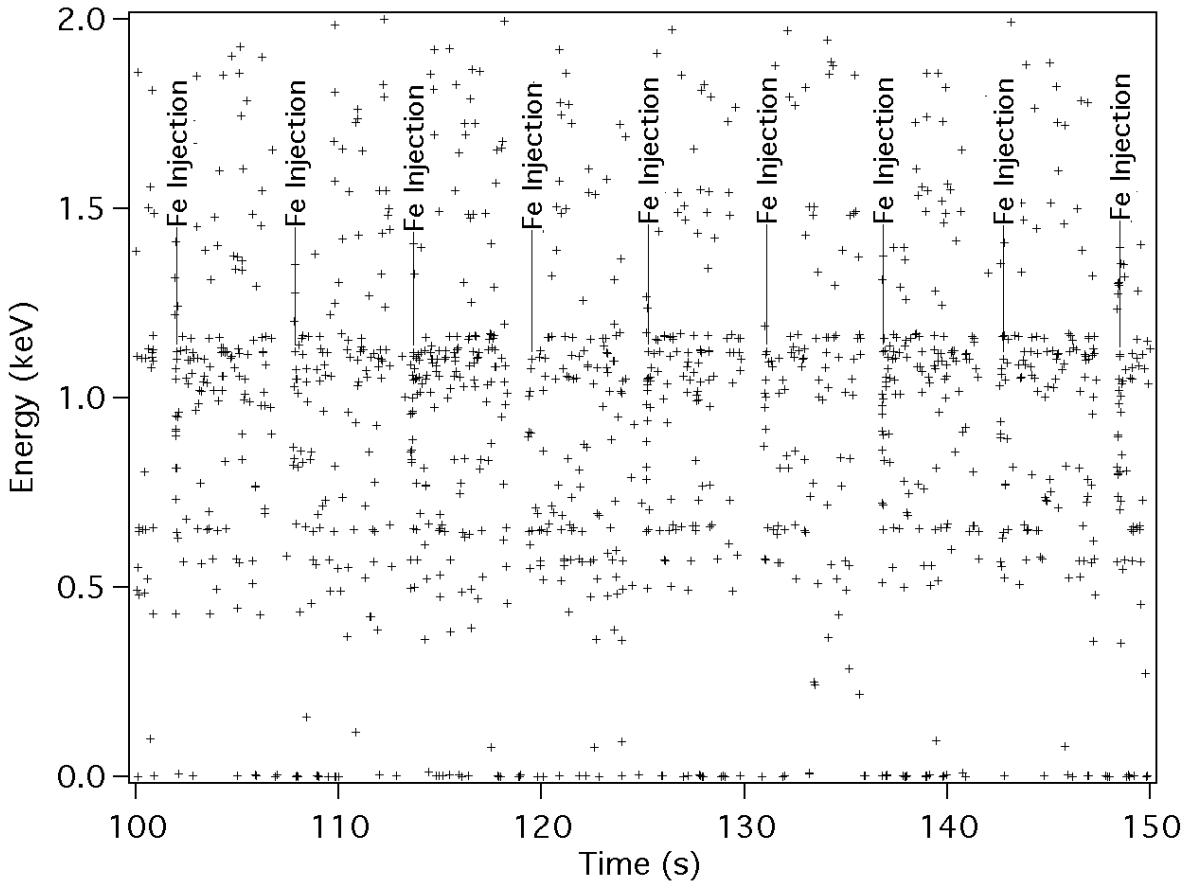
Fe Injection
Fe Injection
Fe Injection
Fe Injection
Fe Injection
Fe Injection
Fe Injection
Fe Injection
Fe Injection
Energy (keV)
2.0
1.5
1.0
0.5
0.0
100
110
120
130
140
150
Time (s)

Figure 9 a-b:

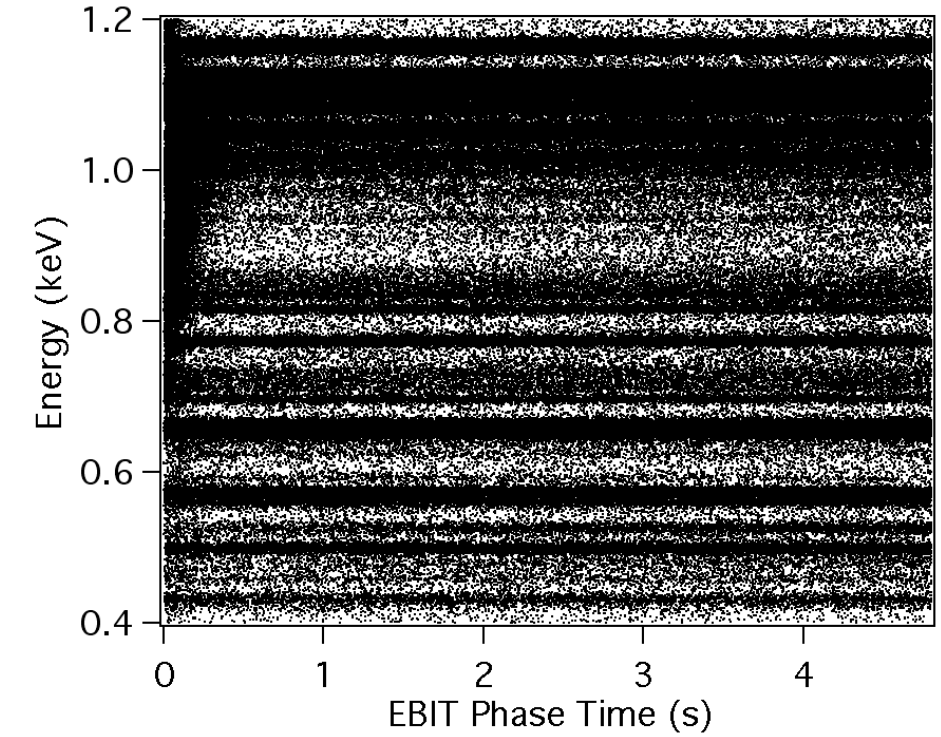
1.2
1.0
0.8
0.6
0.4
Energy (keV)
0
1
2
3
4
EBIT Phase Time (s)

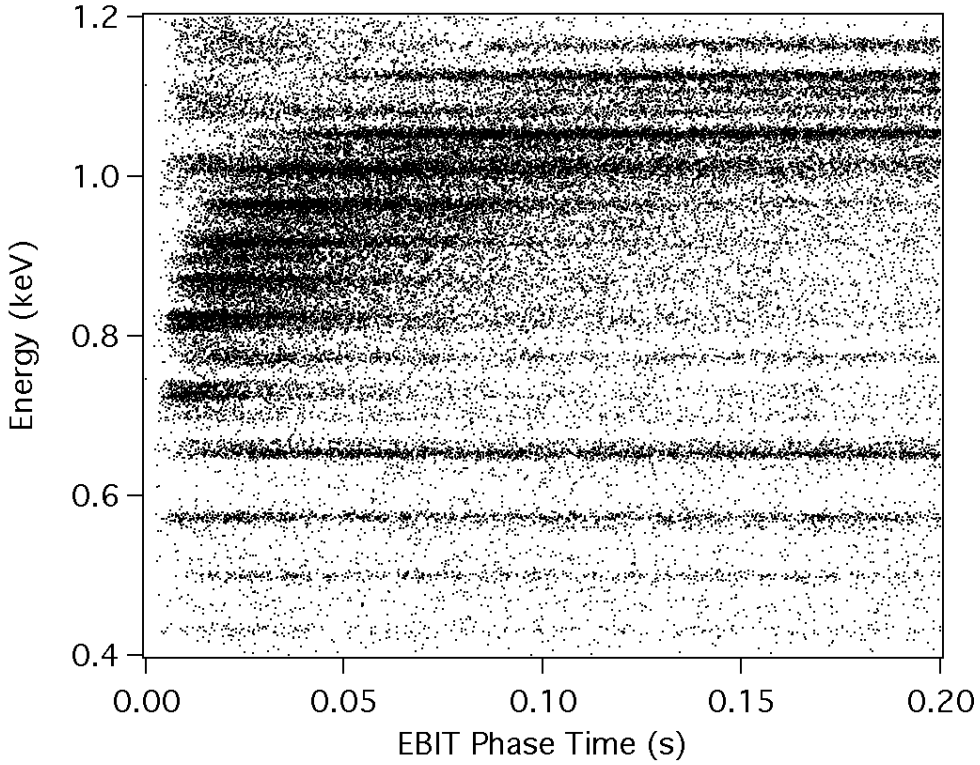
1.2
1.0
0.8
0.6
0.4
Energy (keV)
0.00
0.05
0.10
0.15
0.20
EBIT Phase Time (s)

Figure 10:

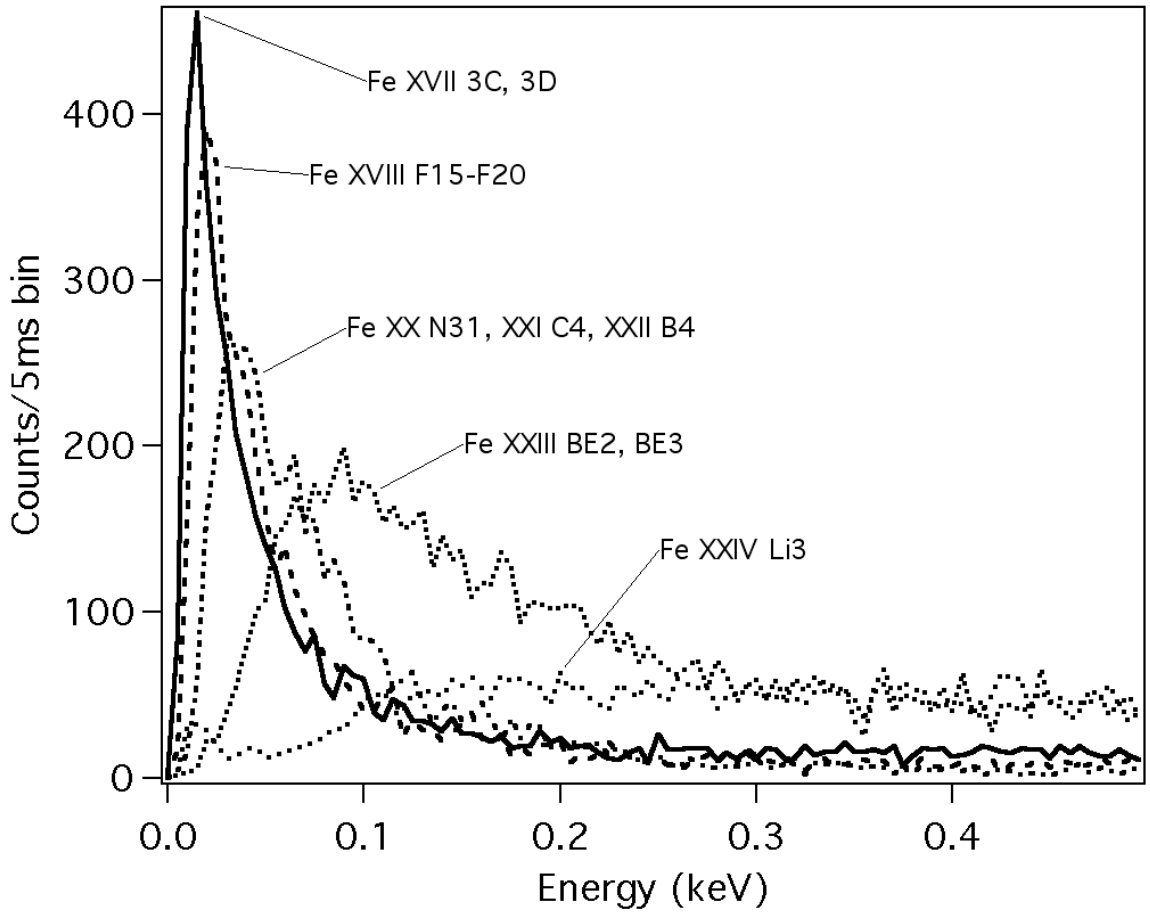
Fe XVII 3C, 3D
Fe XVIII F15-F20
Fe XX N31, XXI C4, XXII B4
Fe XXIII BE2, BE3
Fe XXIV Li3
Counts/5ms bin
0
100
200
300
400
0.0
0.1
0.2
0.3
0.4
Energy (keV)

Figure 11 a-b:

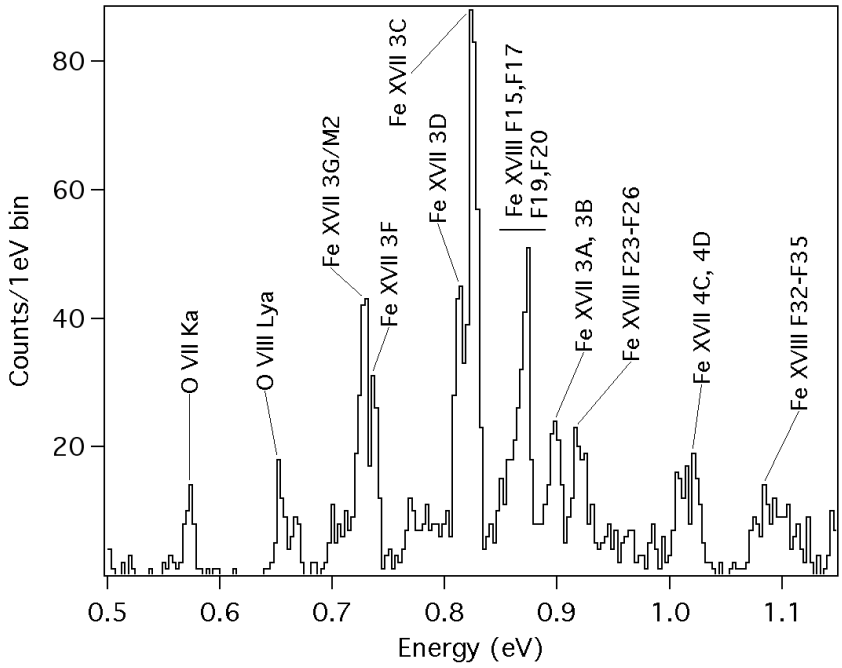
Counts/1eV bin
Energy (eV)
O VII Ka
O VIII Lya
Fe XVII 3G/M2
Fe XVII 3F
Fe XVII 3C
Fe XVII 3D
Fe XVIII F15,F17
F19,F20
Fe XVII 3A, 3B
Fe XVIII F23-F26
Fe XVII 4C, 4D
Fe XVIII F32-F35

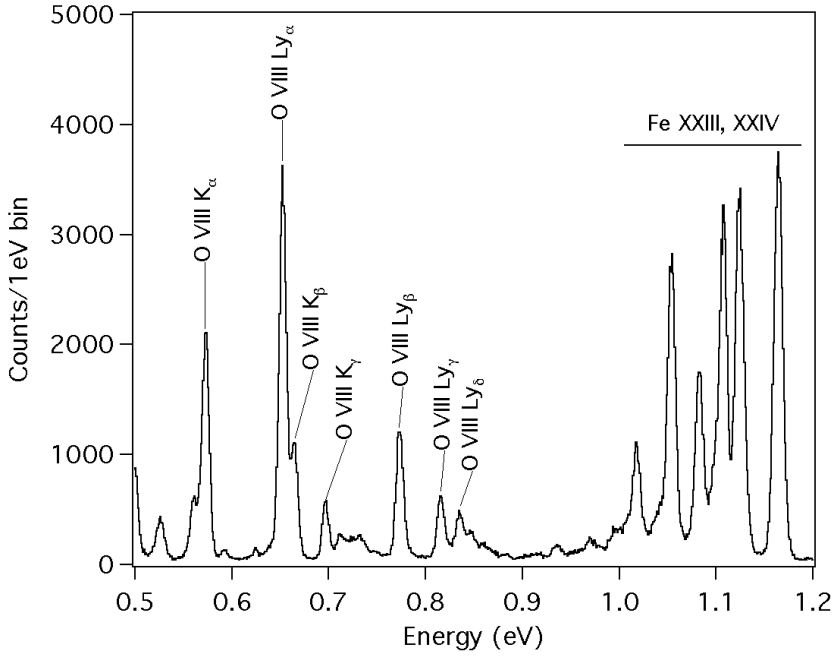
Counts/1eV bin
Energy (eV)
O VIII Kα
O VIII Lyα
O VIII Kβ
O VIII Kγ
O VIII Lyβ
O VIII Lyγ
O VIII Lyδ
Fe XXIII, XXIV

Figure 12:

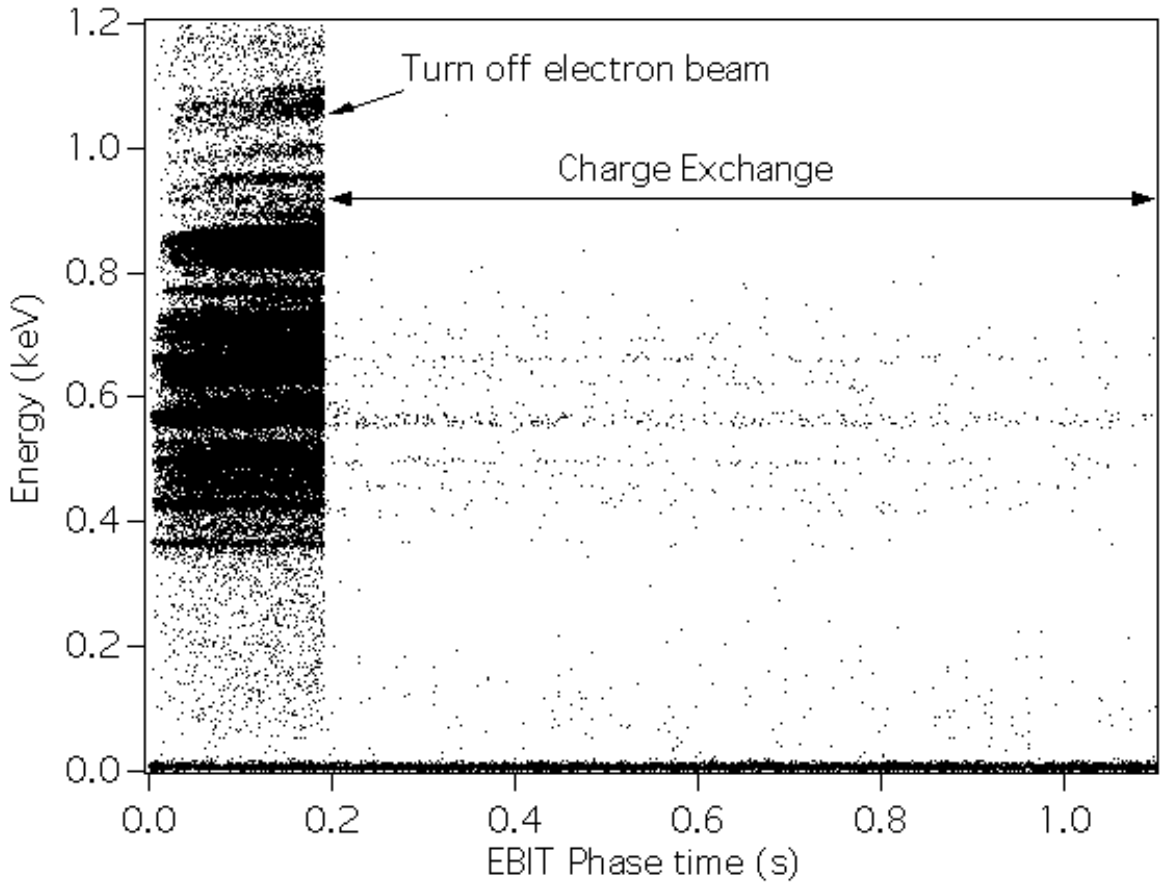
Turn off electron beam
Charge Exchange
Energy (keV)
EBIT Phase time (s)
0.0
0.2
0.4
0.6
0.8
1.0
1.2

Figure 13:

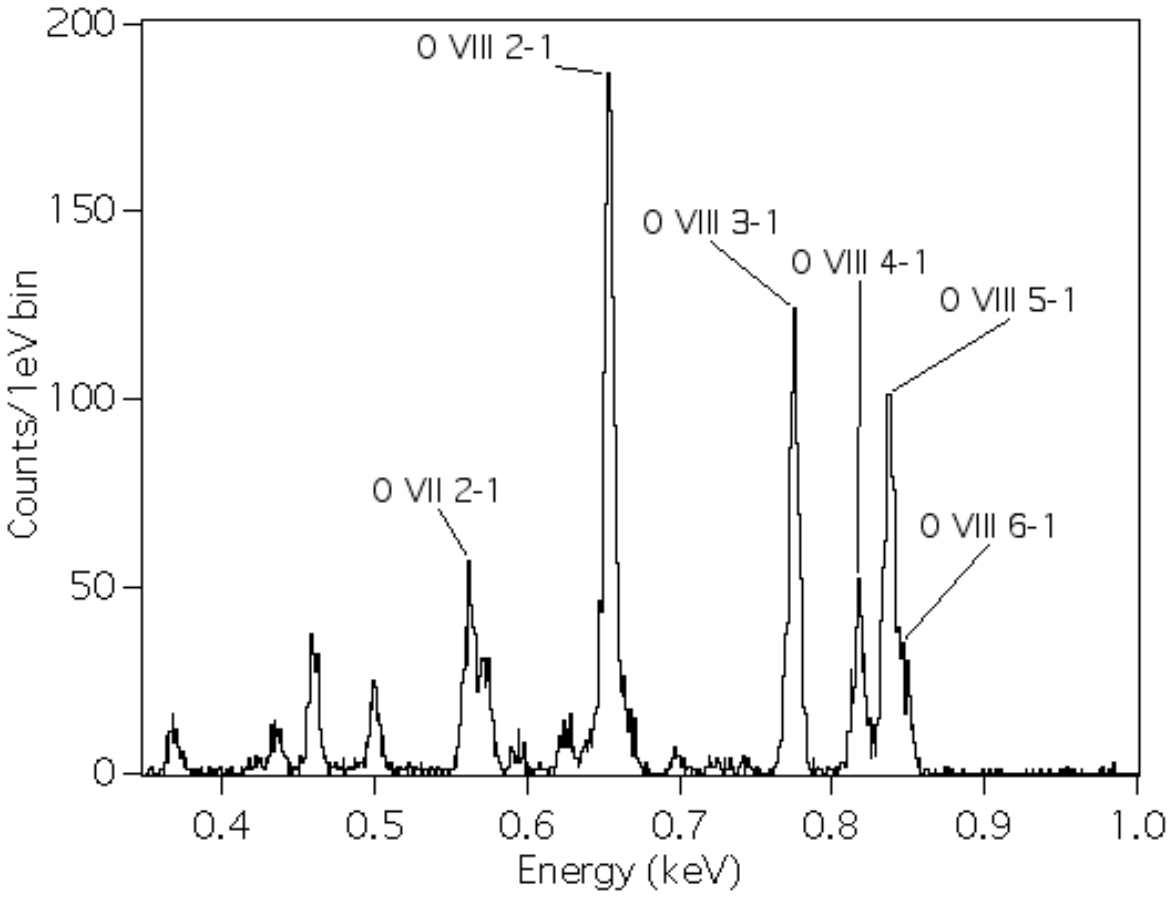
200
150
100
50
0
Counts/1eV bin
O VIII 2-1
O VIII 3-1
O VIII 4-1
O VIII 5-1
O VII 2-1
O VIII 6-1
0.4
0.5
0.6
0.7
0.8
0.9
1.0
Energy (keV)

Figure 14:

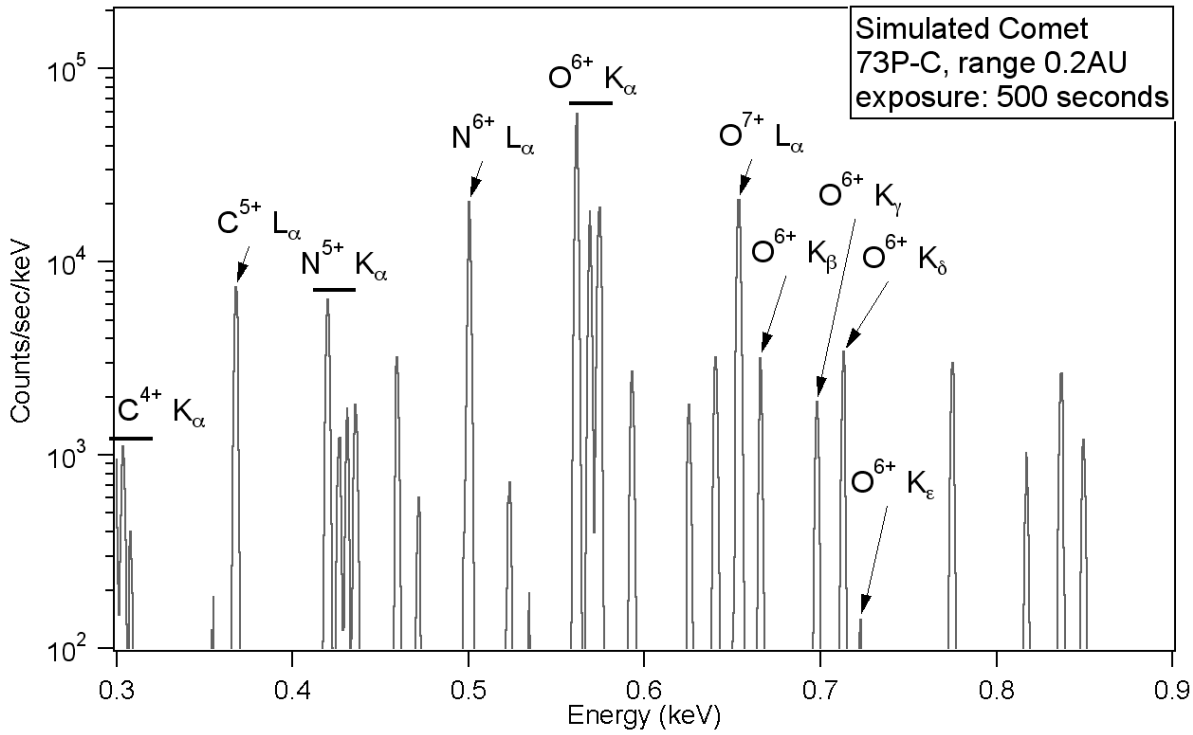
Simulated Comet
73P-C, range 0.2AU
exposure: 500 seconds
Counts/sec/keV
Energy (keV)
C4+ Kα
C5+ Lα
N5+ Kα
N6+ Lα
O6+ Kα
O7+ Lα
O6+ Kβ
O6+ Kγ
O6+ Kδ
O6+ Kε

Figure 15:

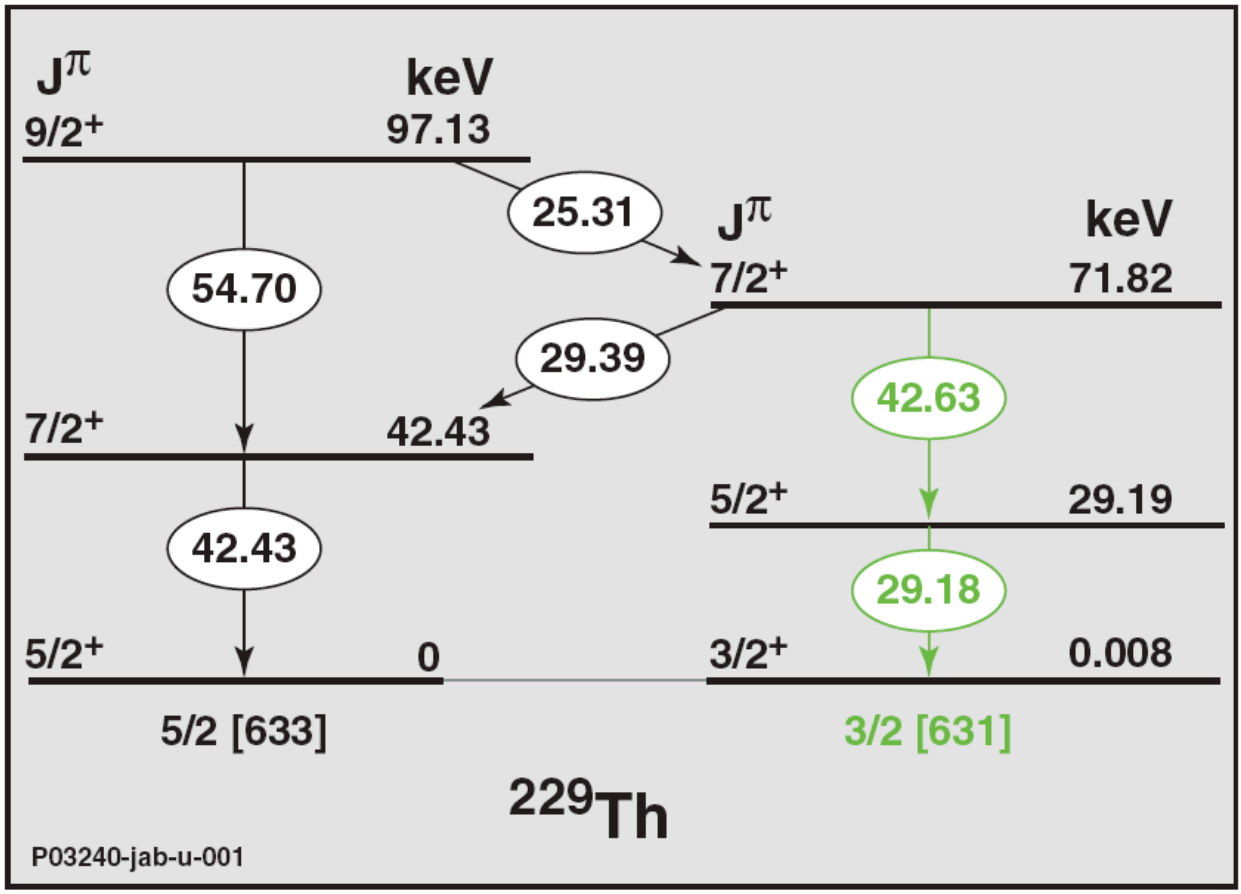
Jπ
keV
9/2+
97.13
25.31
Jπ
keV
54.70
7/2+
71.82
29.39
42.63
7/2+
42.43
5/2+
29.19
42.43
29.18
5/2+
0
3/2+
0.008
5/2 [633]
3/2 [631]
229Th
P03240-jab-u-001

Figure 16:

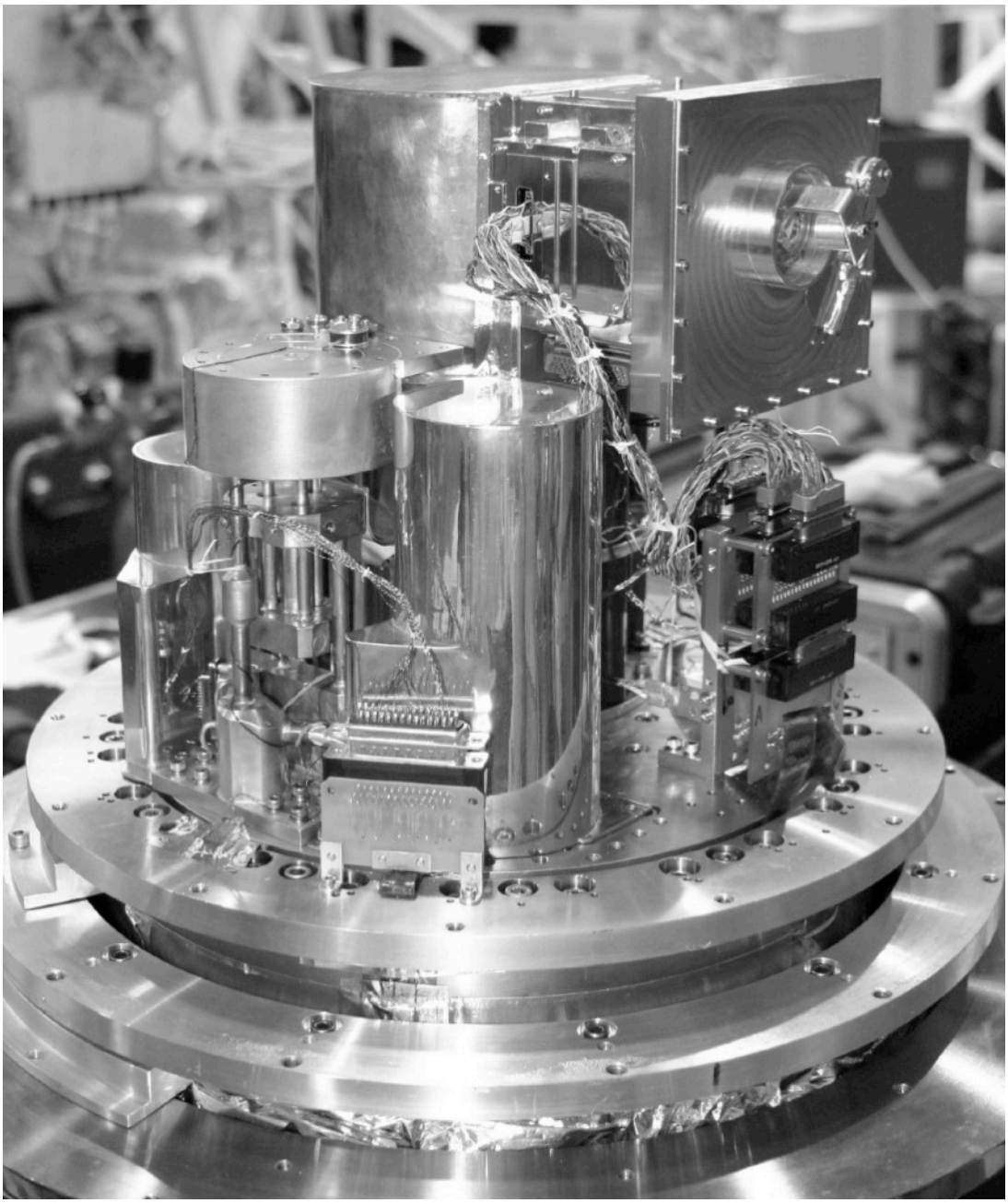

Figure 17:

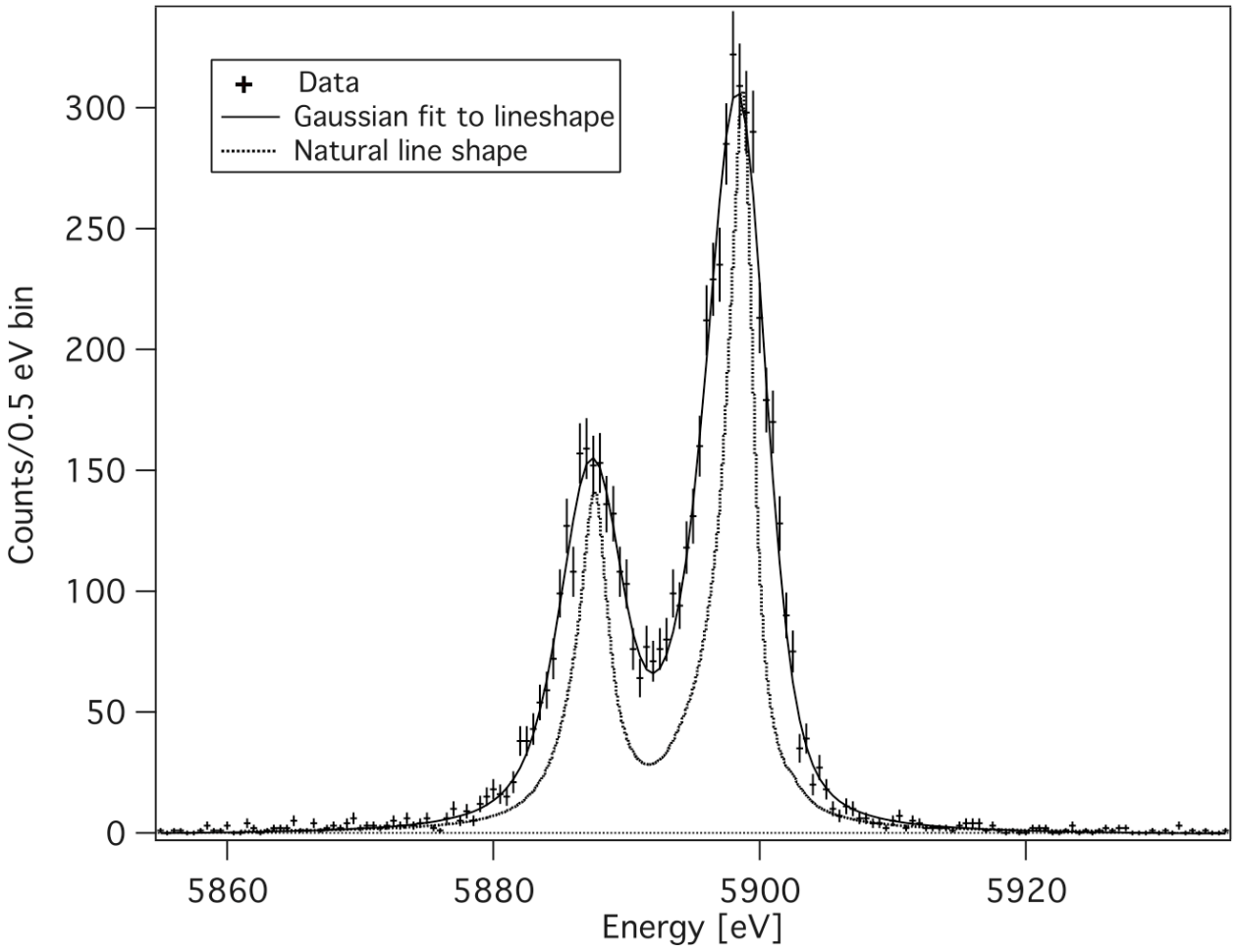
Data
Gaussian fit to lineshape
Natural line shape
Counts/0.5 eV bin
0
50
100
150
200
250
300
5860
5880
5900
5920
Energy [eV]

Figure 18:

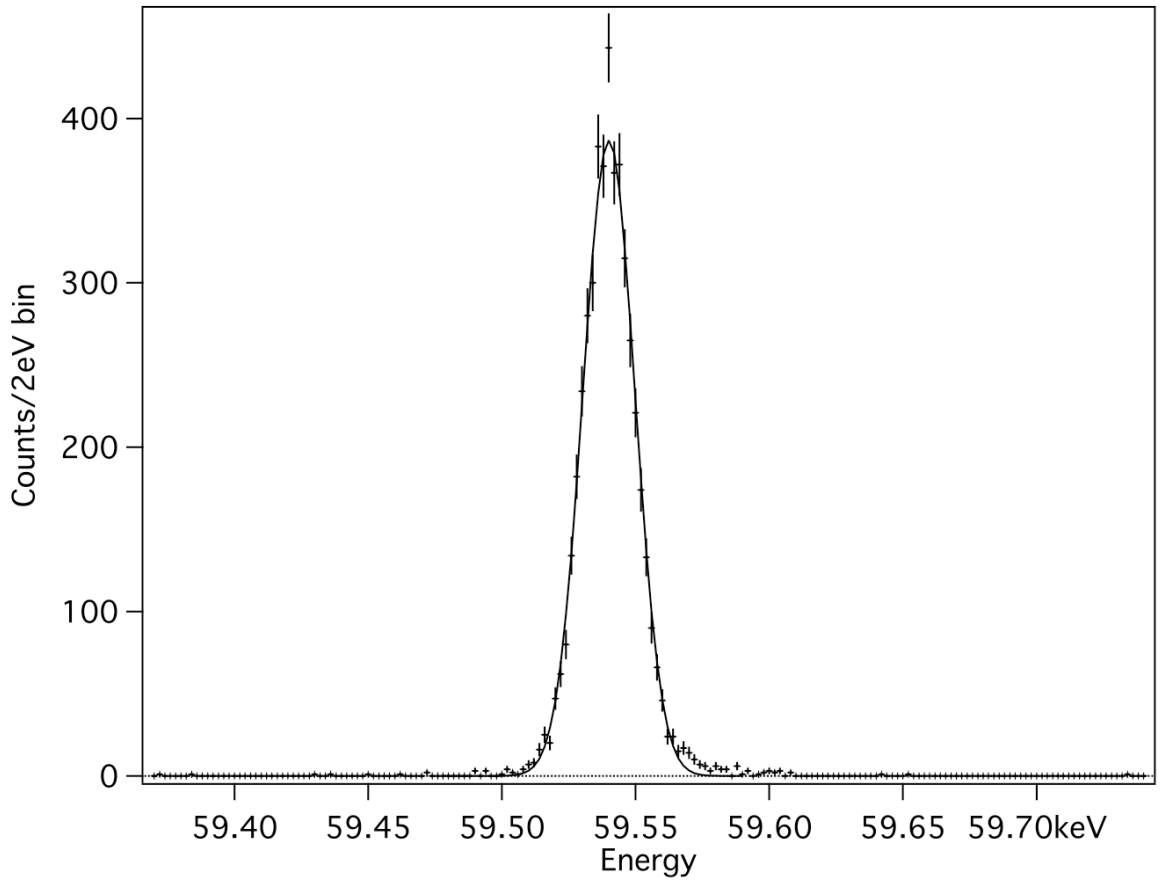
Counts/2eV bin
400
300
200
100
0
59.40
59.45
59.50
59.55
59.60
59.65
59.70keV
Energy